

# Model-Agnostic Cosmological Inference with SDSS-IV eBOSS: Simultaneous Probing for Background and Perturbed Universe

PURBA MUKHERJEE <sup>1</sup> AND ANJAN A SEN <sup>1</sup>

<sup>1</sup>Centre for Theoretical Physics, Jamia Millia Islamia, New Delhi-110025, India.

## ABSTRACT

Here we explore certain subtle features imprinted in data from the completed Sloan Digital Sky Survey IV (SDSS-IV) extended Baryon Oscillation Spectroscopic Survey (eBOSS) as a combined probe for the background and perturbed Universe. We reconstruct the baryon Acoustic Oscillation (BAO) and Redshift Space Distortion (RSD) observables as functions of redshift, using measurements from SDSS alone. We apply the Multi-Task Gaussian Process (MTGP) framework to model the interdependencies of cosmological observables  $D_M(z)/r_d$ ,  $D_H(z)/r_d$ , and  $f\sigma_8(z)$ , and track their evolution across different redshifts. Subsequently, we obtain constrained three-dimensional phase space containing  $D_M(z)/r_d$ ,  $D_H(z)/r_d$ , and  $f\sigma_8(z)$  at different redshifts probed by the SDSS-IV eBOSS survey. Furthermore, assuming the  $\Lambda$ CDM model, we obtain constraints on model parameters  $\Omega_m$ ,  $H_0 r_d$ ,  $\sigma_8$  and  $S_8$  at each redshift probed by SDSS-IV eBOSS. This indicates redshift-dependent trends in  $H_0$ ,  $\Omega_m$ ,  $\sigma_8$  and  $S_8$  in the  $\Lambda$ CDM model, suggesting a possible inconsistency in the  $\Lambda$ CDM model. Ours is a template for model independent extraction of information for both background and perturbed Universe using a single galaxy survey taking into account all the existing correlation between background and perturbed observables and this can be easily extended to future DESI-3YR as well as Euclid results.

*Keywords:* Cosmology (343) – Baryon acoustic oscillations (138) – Dark energy(351) – Cosmological parameters(339) – Gaussian Processes regression(1930)

## 1. INTRODUCTION

The  $\Lambda$ CDM model has long been the cornerstone of modern cosmology, providing a robust framework to explain diverse phenomena (Perlmutter et al. 1999; Riess et al. 1998; Blanchard et al. 2024; Peebles 2024), such as the temperature and polarization fluctuations of the cosmic microwave background (CMB) (Ade et al. 2016; Aghanim et al. 2020; Aiola et al. 2020; Tristram et al. 2024), the large-scale structure of the Universe (Aubourg et al. 2015; Alam et al. 2017, 2021; Adame et al. 2024a), and the distance-redshift relation of type Ia supernovae (SNIa) (Betoule et al. 2014; Scolnic et al. 2018; Brout et al. 2022; Abbott et al. 2024). Despite its success,  $\Lambda$ CDM faces theoretical and observational challenges: theoretical concerns include the unresolved nature of dark matter (Gaitskill 2004; Akerib et al. 2017), the cosmological constant and the cosmic coincidence problem (Weinberg 1989; Sahni & Starobinsky 2000; Carroll 2001; Padmanabhan 2003; Peebles & Ratra 2003). Observationally, tensions such as the  $> 5\sigma$  Hubble constant discrepancy ( $H_0$ ) (Hazra et al. 2015; Verde et al. 2019; Riess 2019; Riess et al. 2022; Di Valentino et al. 2021a; Brieden et al. 2023; Freedman & Madore 2023; Efstathiou 2024) between local distance ladder measurements and CMB-inferred values, as well as the  $\sim 2 - 2.5\sigma$  amplitude of matter fluctuations ( $S_8$ ) (Di Valentino et al. 2021b; Heymans et al. 2021; Abbott et al. 2022; Li et al. 2023) tension between early CMB data and weak lensing surveys, remain unresolved. Recent observations by the James Webb Space Telescope have unveiled massive galaxies at unexpectedly high redshifts ( $z \sim 15$ ) (Labbe et al. 2023; Boylan-Kolchin 2023), further challenging the concordance framework.

Central to these investigations is understanding the energy composition of the Universe, the mechanisms driving cosmic expansion, and the growth of cosmic structures. To accomplish this, scientific models must deliver predictions that are both

consistent with and relevant to these observations (Bull et al. 2016; Di Valentino et al. 2021c; Abdalla et al. 2022; Perivolaropoulos & Skara 2022). In cosmology, redshift  $z$  acts as a proxy for time, making it vital to examine the  $\Lambda$ CDM parameters across redshift bins (Wong et al. 2020; Millon et al. 2020; Krishnan et al. 2020, 2021; Krishnan & Mondol 2022; Dainotti et al. 2021; Colgáin et al. 2022; Hu & Wang 2022; Jia et al. 2023; Colgáin et al. 2024; Vagnozzi 2023; Risaliti & Lusso 2019; Lusso et al. 2020; Yang et al. 2020; Khadka & Ratra 2020; Pastén & Cárdenas 2023; Adil et al. 2023; Akarsu et al. 2024; Artis et al. 2024; Qu et al. 2024). For instance, trends of  $H_0$  decreasing and  $\Omega_m$  increasing, along with an increase of  $\sigma_8$  and  $S_8$  values from low to high  $z$  reported in some recent studies, challenge the fundamental assumption of constancy of model parameters (Krishnan et al. 2021; Krishnan & Mondol 2022). These studies hint at possible missing physics at specific epochs, underscoring the importance of identifying redshift ranges where  $\Lambda$ CDM may break down. Such insights are essential for refining cosmological models and advancing our understanding of the Universe's evolution.

In this work, we analyze data exclusively from the completed Sloan Digital Sky Survey (SDSS)-IV extended Baryon Oscillation Spectroscopic Survey (eBOSS) (Alam et al. 2021), which has been instrumental in advancing cosmological analyses. The BOSS and eBOSS surveys have pioneered the use of Baryon Acoustic Oscillations (BAO) (Eisenstein & Hu 1998) and Redshift Space Distortions (RSD) (Guzzo et al. 1997) to probe the Universe. Herein, we consider data from spectroscopic galaxy and quasar samples spanning four generations of SDSS, including SDSS MGS (Howlett et al. 2015), BOSS galaxies (Alam et al. 2017), eBOSS LRGs (Bautista et al. 2020; Gil-Marín et al. 2020), eBOSS ELGs (Tamone et al. 2020; de Mattia et al. 2021), and eBOSS quasars (Hou et al. 2020; Neveux et al. 2020), as well as Ly- $\alpha$  auto- and cross-correlation measurements from BOSS and eBOSS (du Mas des Bourboux et al. 2020). By focusing solely on SDSS data, we avoid potential conflicts that may be present among datasets from disparate sources. This single-survey approach ensures that our results are less affected by inter-survey calibration errors, systematic uncertainties, modeling discrepancies and external biases that can complicate multi-survey analyses.

Our analysis focuses on reconstructing BAO and RSD observables as a function of redshift. BAO features, observed in both transverse and line-of-sight directions, constrain cosmological distances, such as transverse comoving distance  $D_M(z)/r_d$  and Hubble distance  $D_H(z)/r_d$ . Meanwhile, RSD effects (Kaiser 1987), caused by the bulk motion of matter in gravitational potential wells, provide insights into structure formation through  $f\sigma_8$ , a parameter quantifying the peculiar velocity fields. To this end, we employ the Multi-Task Gaussian Process (MTGP) (Caruana 1998; Rasmussen & Williams 2006; Bonilla et al. 2007), a machine learning framework, to reconstruct the evolution of these BAO and RSD observables in a model independent manner as far as the late time cosmology is concerned. MTGP effectively models the complex interdependencies among  $D_M(z)/r_d$ ,  $D_H(z)/r_d$ , and  $f\sigma_8(z)$  measurements, while integrating systematic and statistical uncertainties directly into the covariance matrix. This also helps us to identify any possible presence of redshift-dependent trends in  $H_0$ ,  $\Omega_m$ , and  $S_8$  in  $\Lambda$ CDM. It also paves the way for future similar study using the Dark Energy Spectroscopic Instrument (DESI) Full Shape measurements (Adame et al. 2024b), the direct successor to SDSS, serving as a promising diagnostic tool for upcoming analyses.

This paper is organized as follows: Section 2 outlines the key concepts and models that underpin the study. In section 3 the relevant data and reconstruction techniques used in the study are described. Section 4 highlights the outcomes of the reconstruction process, followed by consistency checks for  $\Lambda$ CDM, and a comparison of our findings with complementary datasets to validate their robustness. Finally, we summarize the key insights and potential areas for future research in section 5.

## 2. THEORETICAL FRAMEWORK

On large scales, the Universe is described by the spatially flat, homogeneous, and isotropic Friedmann-Lemaître-Robertson-Walker (FLRW) metric, which governs its background evolution. Within this framework, the *Hubble distance*,

$$D_H(z) = \frac{c}{H(z)}, \quad (1)$$

serves as a characteristic scale that relates the expansion rate of the Universe to distances, where  $c$  is the speed of light and  $H(z)$  is the Hubble parameter at redshift  $z$ . At the present epoch, this reduces to  $D_H(z=0) = \frac{c}{H_0}$ , where  $H_0$  is the Hubble constant. Additionally, the *comoving distance*,  $D_M$ , quantifies the separation between two points in the Universe while accounting for its expansion. For a source at redshift  $z$ , it is defined as

$$D_M(z) = c \int_0^z \frac{dz'}{H(z')}. \quad (2)$$

These distances provide a foundation for interpreting cosmological observations and understanding the large-scale structure of the Universe.

The Hubble parameter  $H(z)$ , which dictates the rate of expansion, is dependent on the underlying cosmological model. In the standard  $\Lambda$ -cold dark matter ( $\Lambda$ CDM) framework, for instance, it is given by

$$H(z) = H_0 \sqrt{\Omega_m(1+z)^3 + \Omega_\Lambda}, \quad (3)$$

where  $\Omega_m$  and  $\Omega_\Lambda$  are the present matter and dark energy density parameters, respectively. This model assumes a spatially flat Universe, with matter and dark energy (described by a cosmological constant) as the primary components driving the evolution of the cosmos. Other cosmological models, such as those that incorporate dynamical dark energy behavior or modifications to gravity, can lead to different functional forms for  $H(z)$ . In these models, the Hubble parameter could be influenced by parameters such as the equation of state of dark energy,  $w(z)$ , or modifications to the Friedmann equations that account for the effects of new physics on the expansion rate (Di Valentino et al. 2021c; Abdalla et al. 2022). Thus, the form of  $H(z)$  is a key signature of the cosmological model in question and plays a crucial role in interpreting observational data.

The evolution of cosmic structures is governed by the dynamics encoded in the Hubble parameter, which directly impacts the growth rate of perturbations. At the perturbation level, the growth rate of cosmic structures provides a key insight into the evolution of matter density fluctuations and the underlying cosmological model. It is commonly expressed through the observable  $f\sigma_8$ , which combines the linear growth rate of structures,  $f$ , with  $\sigma_8$ , the root-mean-square (rms) fluctuation of the matter density field in spheres of radius  $8 h^{-1}$  Mpc.

The growth rate  $f$  is defined as,

$$f = \frac{d \ln D(a)}{d \ln a} = -(1+z) \frac{D'(z)}{D(z)}, \quad (4)$$

where  $D(a)$  is the linear growth factor. Under general relativity,  $f$  can often be approximated as  $f \approx \Omega_m(a)^\gamma$ , where  $\Omega_m(a)$  is the matter density parameter at scale factor  $a$ , and  $\gamma$  is the growth index, typically around  $\gamma \approx 0.55$ . The parameter  $\sigma_8$  quantifies the amplitude of matter density fluctuations and is influenced by the normalization of the initial power spectrum, defined as

$$\sigma_8(z) = \sigma_8(z=0)D(z). \quad (5)$$

Thus, the product  $f\sigma_8$  serves as a valuable probe, combining information on the rate of structure formation and the amplitude of clustering.

### 3. DATA AND METHODOLOGY

The BAO observations probe the large-scale structure of the Universe, providing insights into its geometry and the growth of structures. These observations are quantified using normalized distances relative to the sound horizon at the baryon drag epoch, denoted  $r_d$ , which is the distance sound waves travelled from the Big Bang to the epoch of baryon drag (Eisenstein & Hu 1998), defined as

$$r_d = \int_{z_d}^{\infty} \frac{c_s(z)}{H(z)} dz, \quad (6)$$

where  $z_d$  is the redshift of the drag epoch and  $c_s$  is the sound speed.

In spectroscopic surveys, the BAO feature appears along both the line of sight and the transverse direction. Along the line of sight, the redshift interval  $\Delta z$  directly measures the Hubble parameter  $H(z) = \frac{c\Delta z}{r_d}$ , with the Hubble distance  $D_H(z)$ . In the transverse direction, the BAO scale corresponds to an angular separation  $\Delta\theta$ , enabling the estimation of the comoving angular diameter distance  $D_M(z) = \frac{r_d}{\Delta\theta}$ . Galaxy redshift measurements from spectroscopic BAO surveys also reveal anisotropic clustering, influenced by the Redshift Space Distortion (RSD) (Kaiser 1987; Guzzo et al. 1997). The RSD effect, driven by the growth of structure and peculiar velocities, introduces additional redshifts along the line of sight, leading to anisotropic clustering, which is tied to the growth rate  $f\sigma_8$ . Together, BAO and RSD measurements,  $\frac{D_M(z)}{r_d}$ ,  $\frac{D_H(z)}{r_d}$ , and  $f\sigma_8(z)$ , can provide robust constraints on the expansion history and structure growth of the Universe.

In this study, we employ the Multi-Task Gaussian Process (MTGP) (Haridasu et al. 2018; Perenon et al. 2021; Mukherjee & Sen 2024; Dinda & Maartens 2024), a machine learning technique, to analyze the evolution of BAO and RSD observables across multiple generations of SDSS data, spanning a redshift range of  $0 < z < 2.34$ . The data compilation includes measurements from various tracers in different redshift intervals, summarized in Table 1. Unlike traditional approaches that combine these observations with external datasets, viz. Planck (Aghanim et al. 2020; Tristram et al. 2024) or Type Ia supernovae (Brout et al. 2022; Abbott et al. 2024), or the informed use of cosmological priors (Peirone et al. 2017; Patel et al. 2024; Payeur et al. 2024), we focus on directly extracting features from the BAO and RSD measurements within the SDSS data alone, ensuring a systematics-minimized analysis.

**Table 1.** Summary of BAO and RSD observables for various tracers in SDSS-IV Data

Tracer	$z_{\text{eff}}$	$D_M(z)/r_d$	$D_H(z)/r_d$	$f\sigma_8(z)$	Reference
MGS	0.15	...	...	$0.53 \pm 0.16$	Howlett et al. (2015)
BOSS Galaxy (low- $z$ )	0.38	$10.27 \pm 0.15$	$24.89 \pm 0.58$	$0.497 \pm 0.045$	Alam et al. (2017)
BOSS Galaxy (high- $z$ )	0.51	$13.38 \pm 0.18$	$22.43 \pm 0.48$	$0.459 \pm 0.038$	Alam et al. (2017)
eBOSS LRG	0.698	$17.65 \pm 0.30$	$19.78 \pm 0.46$	$0.473 \pm 0.041$	Alam et al. (2021)
eBOSS QSO	1.48	$30.21 \pm 0.79$	$13.23 \pm 0.47$	$0.462 \pm 0.045$	Hou et al. (2020)
Ly $\alpha$ QSO	2.334	$37.5 \pm 1.2$	$8.99 \pm 0.19$	...	du Mas des Bourboux et al. (2020)

While a single-task GP (see Holsclaw et al. (2010, 2011); Seikel et al. (2012); Shafieloo et al. (2012); Mukherjee (2022) and references therein), is effective for reconstructing individual functions from independent datasets, it does not account for the shared information between observables derived from overlapping datasets. In our case, the observables  $D_M(z)/r_d$ ,  $D_H(z)/r_d$ , and  $f\sigma_8(z)$ , derived from galaxies, quasars, and Ly- $\alpha$  forests across different redshift ranges, exhibit interdependencies and are influenced by common systematics and statistical uncertainties, governed by the same underlying physics. Treating each observable independently risks underestimating uncertainties and leading to suboptimal reconstructions.

The MTGP framework overcomes this limitation by modeling redshift-dependent relationships between the observables - their auto-correlations and cross-correlations through a joint covariance structure. We use three squared exponential kernels to model the individual functions,

$$k_{i \times i}(z, \tilde{z}) = \sigma_{f_i}^2 \exp \left[ -\frac{(z - \tilde{z})^2}{2l_i^2} \right] \quad \dots i = 1, 2, 3 \quad (7)$$

and a convolution of two kernels

$$k_{i \times j}(z, \tilde{z}) = \sigma_{f_i} \sigma_{f_j} \left( \frac{2l_i l_j}{l_i^2 + l_j^2} \right)^{\frac{1}{2}} \exp \left[ -\frac{(z - \tilde{z})^2}{l_i^2 + l_j^2} \right] \quad \dots i = 1, 2, 3 \quad (8)$$

to capture the correlations between them. Here,  $\{\sigma_{f_i}, l_i, \dots i = 1, 2, 3\}$  are the hyperparameters of the kernel, which are trained by marginalizing over the log-likelihood,

$$\ln \mathcal{L}(\{\sigma_{f_i}, l_i, \dots i = 1, 2, 3\}) = -\frac{1}{2} y^T (\tilde{K} + C)^{-1} y - \frac{1}{2} \ln |\tilde{K} + C| - \frac{n}{2} \ln 2\pi. \quad (9)$$

Here,  $n$  is the total number of SDSS data points,  $\tilde{K} = [K_{ij}]$  is the joint MTGP kernel,  $y = \left[ \frac{D_M}{r_d} \quad \frac{D_H}{r_d} \quad f\sigma_8 \right]^T$  is the data, and

$$C = \begin{bmatrix} \text{cov}(D_M/r_d, D_M/r_d) & \text{cov}(D_M/r_d, D_H/r_d) & \text{cov}(D_M/r_d, f\sigma_8) \\ \text{cov}(D_H/r_d, D_M/r_d) & \text{cov}(D_H/r_d, D_H/r_d) & \text{cov}(D_H/r_d, f\sigma_8) \\ \text{cov}(f\sigma_8, D_M/r_d) & \text{cov}(f\sigma_8, D_H/r_d) & \text{cov}(f\sigma_8, f\sigma_8) \end{bmatrix},$$

is the combined data covariance in block form. Finally, the predicted mean and covariance are,

$$\bar{f}^* = \tilde{K}^* [\tilde{K} + C]^{-1} y \quad (10)$$

$$\text{cov} f^* = \tilde{K}^{**} - \tilde{K}^* [\tilde{K} + C]^{-1} \tilde{K}^{*T}. \quad (11)$$

Therefore, our approach ensures a cohesive reconstruction by accounting for the interdependencies between the tracers and properly incorporating both systematic errors and statistical uncertainties into the covariance matrix. By leveraging these correlations, the MTGP framework enables a more accurate reconstruction of the redshift-dependent trends in the observables.



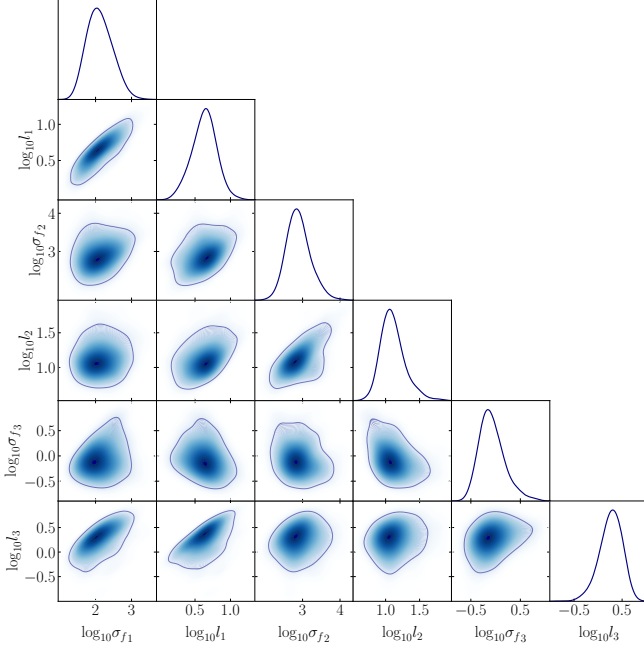


**Figure 1.** Triangle plot for MTGP hyperparameter samples.

**Table 2.** Hyperparameter values with best-fit and mean with  $1\sigma$ .

Hyperparameters	Priors	Best-Fit	Mean with $1\sigma$
$\log_{10}\sigma_{f1}$	$\mathcal{U}[-5, 5]$	2.115	$2.088^{+0.411}_{-0.337}$
$\log_{10}l_1$	$\mathcal{U}[-5, 5]$	0.629	$0.640^{+0.157}_{-0.187}$
$\log_{10}\sigma_{f2}$	$\mathcal{U}[-5, 5]$	2.891	$2.869^{+0.336}_{-0.291}$
$\log_{10}l_2$	$\mathcal{U}[-5, 5]$	1.107	$1.085^{+0.189}_{-0.154}$
$\log_{10}\sigma_{f3}$	$\mathcal{U}[-5, 5]$	-0.075	$-0.104^{+0.273}_{-0.218}$
$\log_{10}l_3$	$\mathcal{U}[-5, 5]$	0.265	$0.281^{+0.229}_{-0.255}$

#### 4. ANALYSIS AND DISCUSSIONS

We undertake MTGP regression on the joint SDSS BAO+RSD data using the `tinygp`<sup>1</sup> (Foreman-Mackey et al. 2024) module, implementing a Bayesian MCMC analysis with `jax`<sup>2</sup> (Bradbury et al. 2018) and `numpyro`<sup>3</sup> (Phan et al. 2019; Bingham et al. 2019). For this, we assume uniform flat priors on the kernel hyperparameters, as detailed in Table 1. The signal amplitudes  $\log_{10}\sigma_{f_i}$  and length scales  $\log_{10}l_i$  for each observable are optimized within the prior range of  $[-5, 5]$ . Large values of  $\sigma_f$  for the two BAO observables  $D_M/r_d$  and  $D_H/r_d$  indicate strong signal strengths, leading to substantial contributions from these components to the overall covariance. In contrast, a lower  $\sigma_f$  value for the RSD observable  $f\sigma_8$  implies relatively lower variability or weaker correlations, which could stem from the smaller effective sample size or increased uncertainties associated with  $f\sigma_8$  data. The length scales  $l$  exhibit moderate values across all observables, suggesting a balance between the smoothness of the kernel and the flexibility to adapt to redshift-dependent variations in the datasets. The  $1\sigma$  uncertainties around the mean hyperparameter values are relatively small, indicating that the posterior distributions are well-constrained and that the data provide robust constraints on the kernel parameters. The marginalized posterior distributions and the corresponding 2D parameter spaces for the samples are visualized in Fig. 1, generated with `GetDist`<sup>4</sup> (Lewis 2019).

##### 4.1. Result of Reconstruction

Fig. 2 displays six 3D phase spaces, corresponding to six redshift values, showcasing the reconstructed observables  $D_M(z)/r_d$ ,  $D_H(z)/r_d$ , and  $f\sigma_8(z)$  at the  $2\sigma$  confidence level, obtained using the MTGP framework applied to SDSS BAO and RSD data. These plots offer a comprehensive visualization of the interplay between the background and perturbation sectors of cosmology. The MTGP reconstructions are shown in blue regions, whereas Planck  $\Lambda$ CDM predictions are represented in red regions, allowing a direct comparison of their behavior across different redshifts. Each phase portrait captures the relationships between the three predicted observables at a specific redshift, providing a geometric perspective on their mutual correlations within parameter space. Consistent overlap between the blue and red regions indicates agreement between the MTGP reconstruction and  $\Lambda$ CDM, while noticeable deviations while deviations in specific observables may highlight potential tensions or the presence of new physics. For instance,

- At lower redshifts,  $z = 0.15, 0.38, 0.51$  and  $0.698$  the phase spaces exhibit good agreement between the reconstructions and  $\Lambda$ CDM predictions.

<sup>1</sup> <https://github.com/dfm/tinygp.git>

<sup>2</sup> <https://github.com/jax-ml/jax.git>

<sup>3</sup> <https://github.com/pyro-ppl/numpyro.git>

<sup>4</sup> <https://github.com/cmbant/getdist.git>

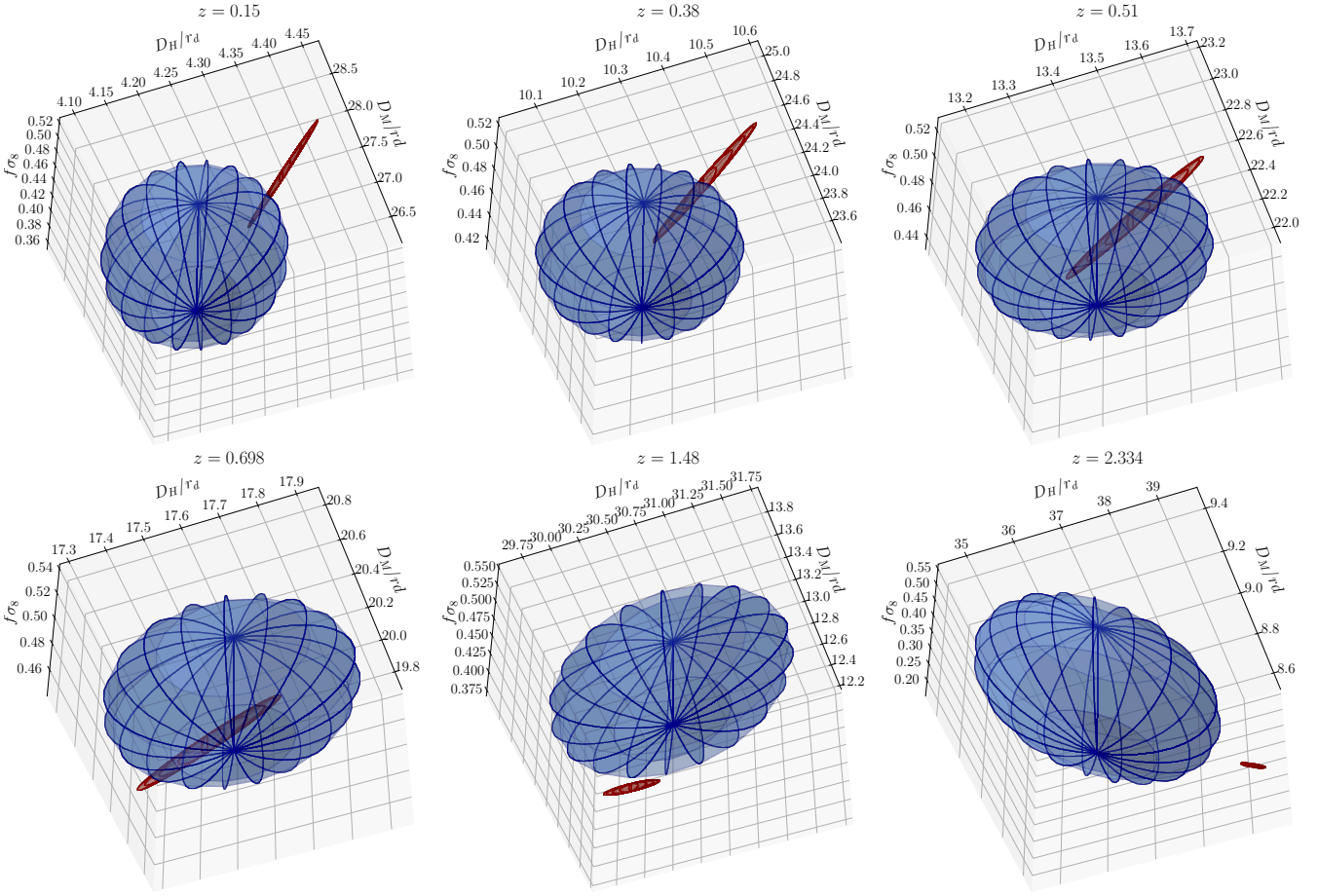


**Figure 2.** 3D phase spaces from the reconstructed functions  $D_M/r_d$ ,  $D_H/r_d$  and  $f\sigma_8$  covering  $2\sigma$  uncertainty at SDSS effective redshifts.

- At higher redshifts  $z = 1.48$  and  $z = 2.334$  noticeable discrepancies from Planck  $\Lambda$ CDM are seen to emerge.

Therefore, these phase spaces are instrumental in analyzing the interplay between the background observables ( $D_M(z)/r_d$  and  $D_H(z)/r_d$ ) and the perturbation observable ( $f\sigma_8(z)$ ), allowing for a joint assessment of the concordance model's performance across redshifts. It helps identify where and how deviations arise, offering insights into potential breakdowns of  $\Lambda$ CDM. It also highlights specific redshifts where the exploration of new physics could be motivated, providing a framework to explain the features observed in the data and guiding investigations beyond  $\Lambda$ CDM.

To better understand the observables when deviations from  $\Lambda$ CDM arise, we plot the reconstructed redshift evolution of the cosmological observables  $D_M(z)/r_d$ ,  $D_H(z)/r_d$ , and  $f\sigma_8(z)$  in Fig. 3. The best-fit lines from MTGP predictions are shown in blue with shaded confidence intervals plot using `fgivenx`<sup>5</sup> (Handley 2018). The black points with error bars represent the observational data, while the red lines (along with the shaded confidence regions) show the corresponding predictions from the Planck 2018  $\Lambda$ CDM model for comparison, offering insights into the consistency and potential tensions between the data and the standard cosmological model. The MTGP reconstruction closely aligns with the data, with well-constrained confidence intervals capturing the uncertainties. By extrapolating the reconstructed  $D_H(z)/r_d$  to  $z = 0$ , we obtain a constraint

<sup>5</sup> <https://github.com/handley-lab/fgivenx.git>

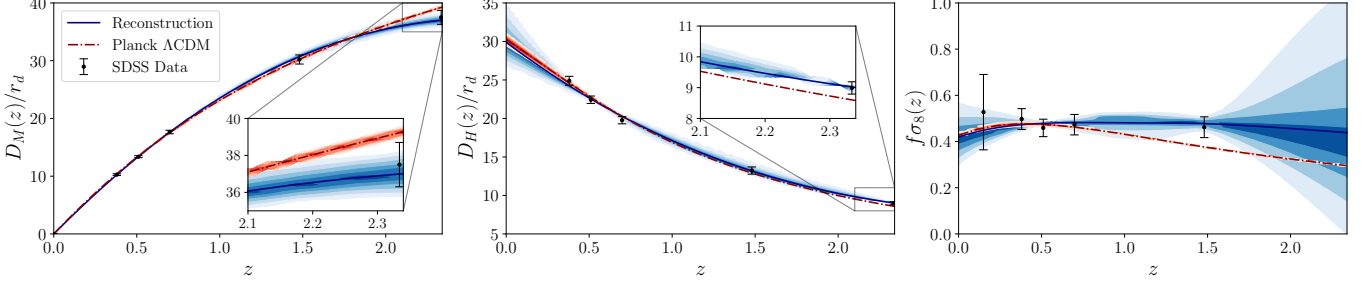


**Figure 3.** Plots for the reconstructed functions  $D_M(z)/r_d$ ,  $D_H(z)/r_d$  and  $f\sigma_8(z)$  [best-fit results with  $1\sigma$  &  $2\sigma$  uncertainties] vs redshift in blue. Planck  $\Lambda$ CDM predictions are in red.

of  $D_H/r_d(z=0) = 29.825 \pm 0.826$ . This leads to a model-independent measurement of  $H_0 r_d = 100.59 \pm 2.78$  in units of 100 km/s. Using the sound horizon  $r_d$  inferred from early-Universe observations (which is completely independent of physics at low redshifts) as obtained by Planck  $r_d = 147.09 \pm 0.26$  Mpc (Aghanim et al. 2020), we derive an inferred value of  $H_0 = 68.38 \pm 1.89$  km Mpc $^{-1}$  s $^{-1}$ . This result lies within  $2\sigma$  of both the Planck  $\Lambda$ CDM determination ( $H_0^{\text{Planck}} = 67.36 \pm 0.54$  km Mpc $^{-1}$  s $^{-1}$  Aghanim et al. (2020)) and the SH0ES local measurement ( $H_0^{\text{SH0ES}} = 73.2 \pm 1.04$  km Mpc $^{-1}$  s $^{-1}$  Riess et al. (2022)). The error in the measured value of  $H_0$  is around 2.76% from SDSS-IV eBOSS solely, given an early Universe Prior. This shows the potential of MTGP framework in determining cosmological parameters in a model-independent way from a single Survey like SDSS-IV eBOSS.

Furthermore, we notice the following trends:

- **Agreement with Planck  $\Lambda$ CDM in lower redshifts:** The reconstructed trends for background observables  $D_M(z)/r_d$  and  $D_H(z)/r_d$ , derived purely from the background expansion history, are consistent with Planck predictions in the redshift range  $z < 1.48$  at the  $1\sigma$  confidence level. The reconstructed  $f\sigma_8(z)$ , which probes the growth of linear perturbations, also agrees with Planck  $\Lambda$ CDM in the redshift range  $z \lesssim 1$ .
- **Deviations in  $f\sigma_8(z)$  at higher redshifts:** A statistically significant deviation exceeding  $2\sigma$  arises in  $f\sigma_8$ , suggesting possible tensions with Planck  $\Lambda$ CDM and hinting at potential new physics affecting the perturbation sector. No such deviations are found in  $D_M(z)/r_d$  and  $D_H(z)/r_d$ , which remain consistent with the Planck baseline model.
- **Anomalies in  $D_M(z)/r_d$  and  $D_H(z)/r_d$  at higher redshifts:** An additional deviation at  $z = 2.334$  is observed in the  $D_M(z)/r_d$  and  $D_H(z)/r_d$  reconstruction relative to the Planck predictions. This feature is difficult to interpret due to the absence of corresponding  $f\sigma_8(z)$  measurements, leaving it unclear whether it signifies new physics or is merely a statistical anomaly.

These trends highlight the standard cosmological model’s consistency at lower redshifts, emphasizing the need for further investigation into the deviations at higher redshifts. The significant  $2\sigma$  deviation at  $z = 1.48$  in  $f\sigma_8(z)$  strongly points to potential tensions with  $\Lambda$ CDM, while the  $z = 2.334$  point may reflect as an outlier in the background sector. Determining whether these anomalies arise from unmodeled systematics, statistical fluctuations, or indications of beyond- $\Lambda$ CDM physics requires additional scrutiny. These findings underscore the need for combining data from both the background and perturbation sectors to fully understand deviations from the standard cosmological framework.

#### 4.2. Consistency checks for $\Lambda$ CDM

In what follows, we fit the parameters of the  $\Lambda$ CDM model to the individual 3D reconstructed phase spaces of the observables  $D_M(z)/r_d$ ,  $D_H(z)/r_d$ , and  $f\sigma_8(z)$  for each redshift bin, using Cobaya<sup>6</sup> (Torrado & Lewis 2021). Table 3 summarizes the resulting parameter estimates, including the best-fit values and the means with their  $1\sigma$  uncertainties for  $H_0 r_d$ ,  $\Omega_m$ ,  $\sigma_8$ , and  $S_8$ . These fits provide a detailed assessment of how the reconstructed datasets at each effective redshift  $z_{\text{eff}}$ , their mutual correlations, comply with the predictions of  $\Lambda$ CDM. It captures how effectively the baseline model explains the intricate interplay between

<sup>6</sup> <https://github.com/CobayaSampler/cobaya.git>

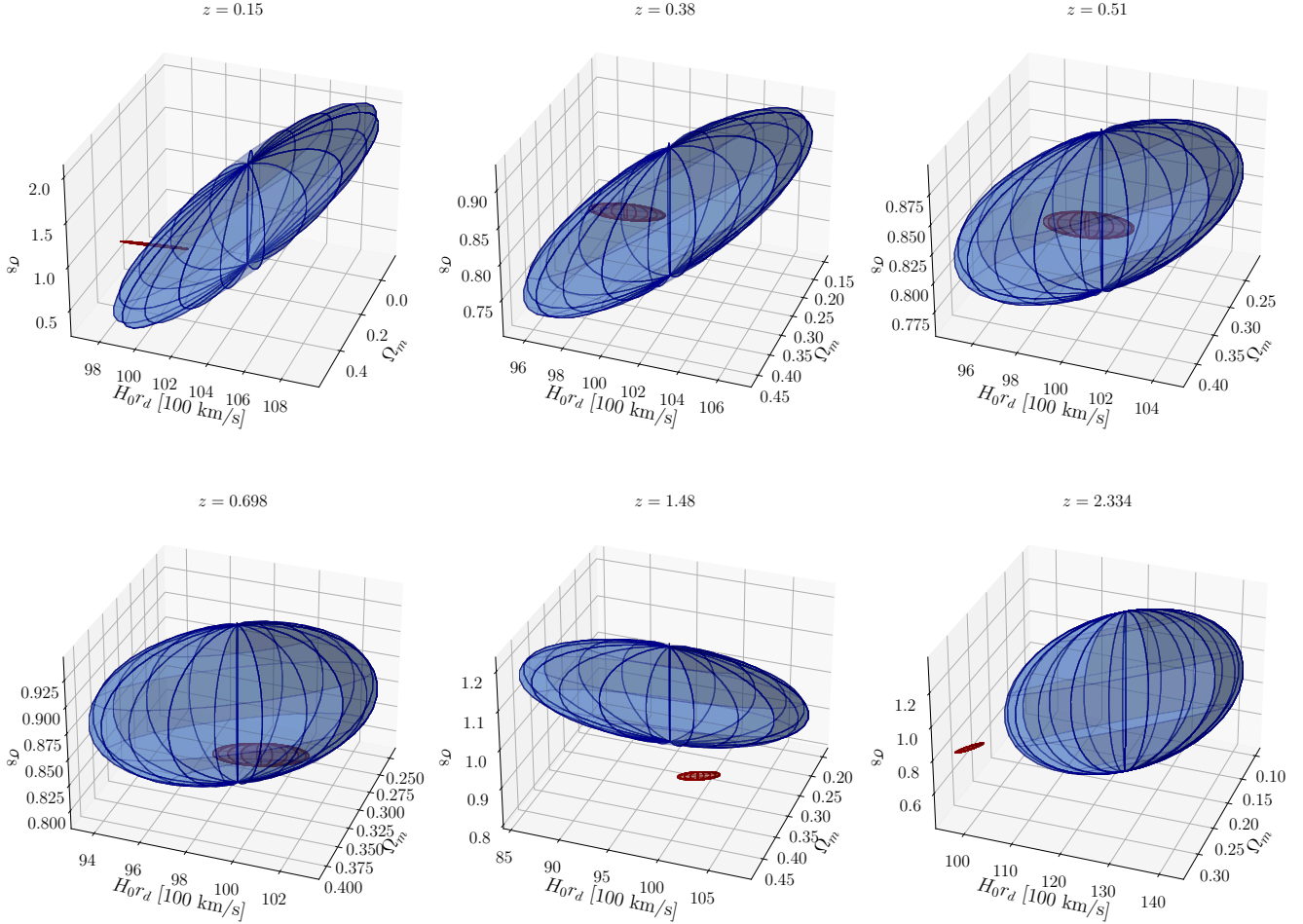


**Figure 4.** 3D phase spaces of the  $\Lambda$ CDM parameters (best-fit with  $2\sigma$  uncertainty) obtained on fitting the  $\Lambda$ CDM model to the reconstructed functions  $D_M/r_d$ ,  $D_H/r_d$  and  $f\sigma_8$  at SDSS effective redshifts in blue. Planck  $\Lambda$ CDM predictions are in red.

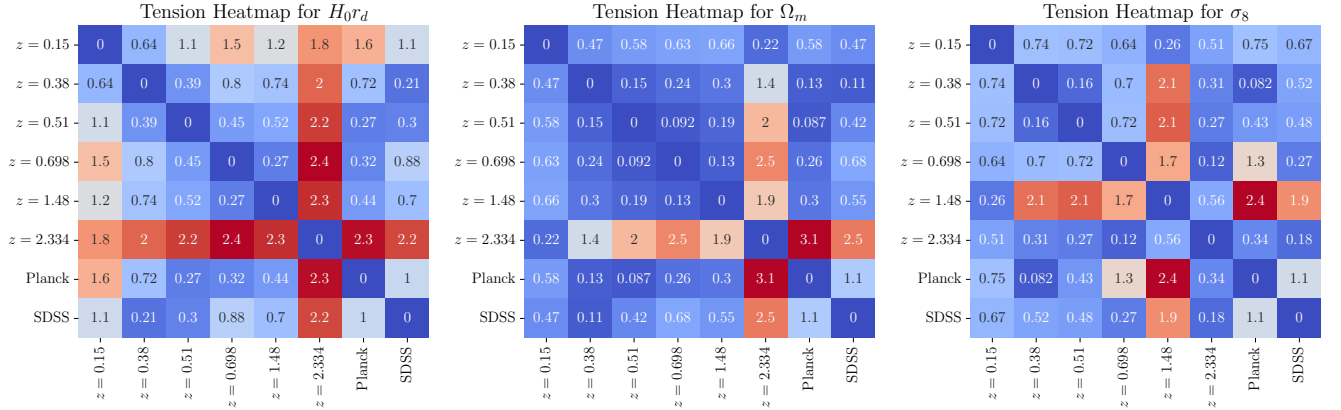
the background and perturbation sectors, offering valuable insights into the trends and potential deviations of the cosmological parameters across redshift as a consistency check for the underlying model.

For completeness, we also plot the 3D phase spaces of the reconstructed  $\Lambda$ CDM parameters ( $H_0 r_d$ ,  $\Omega_m$ , and  $\sigma_8$ ) for six distinct redshift bins  $z = 0.15, 0.38, 0.51, 0.698, 1.48$ , and  $2.334$ . The blue ellipsoids represent the regions constrained by the MTGP reconstructions, while the red markers or compact regions correspond to the Planck  $\Lambda$ CDM predictions. These visualizations serve as a powerful tool to provide a geometric perspective on the correlations and degeneracies between the parameters at each redshift. The ellipsoidal shapes encapsulate the relationships between the background and perturbation sectors, along with their mutual correlations. It also identifies potential deviations or tensions, with notable trends emerging at  $z = 1.48$  and  $z = 2.334$ , where the reconstructed regions show significant departure from the Planck  $\Lambda$ CDM predictions. This suggests that these phase spaces not only validate the model at lower redshifts but also pinpoint redshift ranges where new physics or beyond- $\Lambda$ CDM scenarios may need to be considered.

To better quantify the degree of statistical tension (measured in  $\sigma$ ) in the  $\Lambda$ CDM model parameters  $H_0 r_d$ ,  $\Omega_m$ , and  $\sigma_8$  across different redshifts, we compute the Gaussian Tension. The heatmaps in Fig. 5 reveal that tension becomes increasingly pronounced (exceeding  $2\sigma$ , highlighted in red) at higher redshifts, particularly at  $z = 1.48$  and  $z = 2.334$ , where values diverge significantly from Planck and SDSS predictions. Conversely, regions in blue indicate tensions below  $1\sigma$ . At  $z = 1.48$ ,  $\sigma_8$  notably differs from

**Table 3.** Parameter Estimates for Reconstructed Cosmological Observables  $D_M(z)/r_d$ ,  $D_H(z)/r_d$  and  $f\sigma_8(z)$  assuming  $\Lambda$ CDM model.

Sample	$H_0 r_d$ [in 100 km/s]		$\Omega_m$		$\sigma_8$		$S_8$	
	Best Fit	Mean with $1\sigma$	Best Fit	Mean with $1\sigma$	Best Fit	Mean with $1\sigma$	Best Fit	Mean with $1\sigma$
$z = 0.15$	$103.733 \pm 2.713$	$104.128^{+2.235}_{-3.190}$	$0.220 \pm 0.162$	$0.184^{+0.196}_{-0.120}$	$1.163 \pm 0.469$	$1.003^{+0.711}_{-0.265}$	$0.804 \pm 0.078$	$0.800^{+0.077}_{-0.072}$
$z = 0.38$	$101.226 \pm 2.828$	$101.229^{+2.785}_{-2.819}$	$0.306 \pm 0.076$	$0.302^{+0.078}_{-0.071}$	$0.816 \pm 0.057$	$0.810^{+0.057}_{-0.047}$	$0.812 \pm 0.082$	$0.809^{+0.083}_{-0.078}$
$z = 0.51$	$99.776 \pm 2.429$	$99.760^{+2.445}_{-2.412}$	$0.320 \pm 0.052$	$0.318^{+0.054}_{-0.049}$	$0.827 \pm 0.035$	$0.826^{+0.035}_{-0.035}$	$0.850 \pm 0.073$	$0.848^{+0.074}_{-0.071}$
$z = 0.698$	$98.269 \pm 2.345$	$98.275^{+2.343}_{-2.366}$	$0.326 \pm 0.040$	$0.324^{+0.041}_{-0.038}$	$0.864 \pm 0.039$	$0.865^{+0.039}_{-0.039}$	$0.900 \pm 0.074$	$0.897^{+0.076}_{-0.071}$
$z = 1.48$	$96.626 \pm 5.500$	$96.735^{+5.344}_{-5.622}$	$0.337 \pm 0.070$	$0.328^{+0.075}_{-0.059}$	$1.040 \pm 0.094$	$1.037^{+0.098}_{-0.088}$	$1.104 \pm 0.199$	$1.083^{+0.214}_{-0.173}$
$z = 2.334$	$122.055 \pm 9.804$	$121.998^{+9.768}_{-9.749}$	$0.183 \pm 0.042$	$0.178^{+0.045}_{-0.035}$	$0.894 \pm 0.246$	$0.896^{+0.239}_{-0.245}$	$0.695 \pm 0.208$	$0.684^{+0.210}_{-0.190}$
Planck $\Lambda$ CDM	$99.078 \pm 0.925$	$99.076^{+0.924}_{-0.918}$	$0.315 \pm 0.007$	$0.315^{+0.007}_{-0.007}$	$0.811 \pm 0.006$	$0.811^{+0.006}_{-0.006}$	$0.832 \pm 0.013$	$0.832^{+0.013}_{-0.013}$
SDSS $\Lambda$ CDM	$100.589 \pm 1.204$	$100.593^{+1.188}_{-1.221}$	$0.297 \pm 0.015$	$0.297^{+0.016}_{-0.015}$	$0.850 \pm 0.035$	$0.849^{+0.036}_{-0.034}$	$0.846 \pm 0.042$	$0.845^{+0.042}_{-0.041}$


**Figure 5.** Tension heatmaps between the  $\Lambda$ CDM model parameters  $H_0 r_d$ ,  $\Omega_m$ ,  $\sigma_8$ , across SDSS redshifts. We also show their comparison with the Planck and SDSS baseline results.

those of lower redshifts and Planck/SDSS estimates. At  $z = 2.334$ ,  $H_0 r_d$  and  $\Omega_m$  display  $2\sigma$  tension with other redshifts and Planck/SDSS  $\Lambda$ CDM predictions. Finally, we summarize our findings as follows:

- The parameter  $H_0 r_d$  (in units of 100 km/s) shows a consistent decrease with redshift from  $z = 0.15$  to  $z = 1.48$ , followed by a sharp increase at  $z = 2.334$ , which emerges as an anomaly. Assuming the sound horizon at the drag epoch is constant at  $r_d = 147.09 \pm 0.26$  Mpc, as inferred from early-Universe observations by Planck, the corresponding inferred values of  $H_0$  mirror the trend in  $H_0 r_d$ . Specifically,  $H_0$  is  $70.792^{+1.519}_{-2.169}$  km Mpc $^{-1}$  s $^{-1}$  at  $z = 0.15$ ,  $68.821^{+1.893}_{-1.916}$  km Mpc $^{-1}$  s $^{-1}$  at  $z = 0.38$ ,  $67.822^{+1.662}_{-1.640}$  km Mpc $^{-1}$  s $^{-1}$  at  $z = 0.51$ ,  $66.813^{+1.593}_{-1.609}$  km Mpc $^{-1}$  s $^{-1}$  at  $z = 0.698$ , and  $65.766^{+3.633}_{-3.822}$  km Mpc $^{-1}$  s $^{-1}$  at  $z = 1.48$ . These values are consistent within  $2\sigma$  with both the Planck 2018 estimate and the SH0ES 2021 measurement. In contrast, at  $z = 2.334$ ,  $H_0$  shows a sharp rise to  $82.941^{+6.641}_{-6.628}$  km Mpc $^{-1}$  s $^{-1}$ , standing out as a significant outlier.
- The constraints on  $\Omega_m$  agree with Planck  $\Lambda$ CDM predictions at redshifts  $z = 0.38, 0.51,$  and  $0.698$  within the  $1\sigma$  confidence level. While the best-fit values of  $\Omega_m$  exhibit a gradually increasing trend, this variation is less pronounced compared to the trend observed in  $H_0$ . At  $z = 0.15$ , the precision of  $\Omega_m$  constraints is notably reduced due to the absence of BAO measurements for  $D_M(z)/r_d$  and  $D_H(z)/r_d$  at this redshift, with the only available information coming from the RSD  $f\sigma_8$  measurement from MGS tracers. Additionally, at  $z = 2.334$ ,  $\Omega_m$  is significantly lower compared to the Planck baseline, breaking the increasing trend. This deviation, coupled with the anomalous sharp increase in  $H_0 r_d$  (hence  $H_0$ ), may indicate systematic effects or unexpected physics at this redshift bin. However, this result should be interpreted with caution, as there is no  $f\sigma_8$  measurement from Ly- $\alpha$  tracers to robustly support this finding.
- The  $\sigma_8$  constraints remain relatively stable at redshifts  $z = 0.38, 0.51,$  and  $0.698$ , showing good agreement with the Planck baseline estimates within  $2\sigma$ . At  $z = 0.15$ , the constraints exhibit significant broadening, indicating reduced precision, which can be attributed to the corresponding broadening of  $\Omega_m$  in this redshift bin. At  $z = 1.48$ ,  $\sigma_8$  shows a marked increase, resulting in a tension exceeding  $3\sigma$  compared to Planck  $\Lambda$ CDM. This sharp rise at  $z = 1.48$  could be indicative of



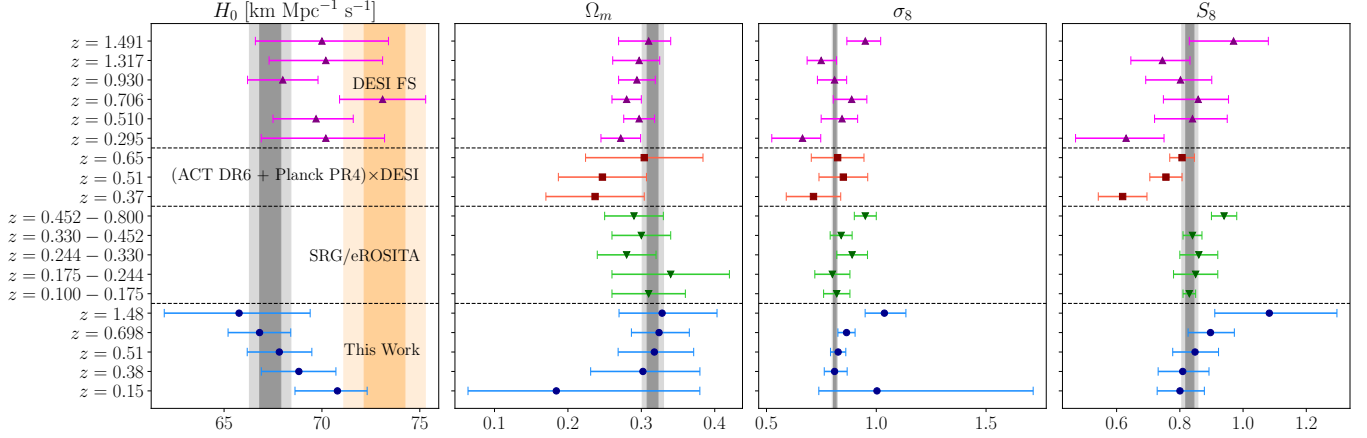


**Figure 6.** Whisker plot showing the redshift-dependence on the inference of cosmological parameters,  $H_0$ ,  $\Omega_m$ ,  $\sigma_8$ , and  $S_8$  obtained from fitting the  $\Lambda$ CDM model to the reconstructed functions. Comparison of these trends across multiple surveys.

some form of rapid transition or deviation from standard cosmological expectations. Conversely, at  $z = 2.334$ ,  $\sigma_8$  appears to decrease, but the large associated uncertainties render this result inconclusive.

- The best-fit values of  $S_8$  exhibit a gradual increasing trend with redshift from  $z = 0.15$  up to  $z = 1.48$ . Within  $1\sigma$ , this pattern mirrors that of  $\sigma_8$ , demonstrating consistency with Planck  $\Lambda$ CDM predictions at lower redshifts  $z = 0.15, 0.38, 0.51$ , and  $0.698$ , followed by a statistically significant  $2\sigma$  rise at  $z = 1.48$  that indicates a potential tension with Planck  $\Lambda$ CDM, pointing toward new physics affecting the perturbation sector. At  $z = 2.334$ ,  $S_8$  shows a subsequent decrease; however, the large uncertainties at this redshift preclude drawing definitive conclusions.
- The blue ellipsoids depict parameter degeneracies and correlations at each redshift, derived from the reconstructed data. For instance,  $H_0 r_d$  and  $\Omega_m$  show strong correlations at lower redshifts ( $z = 0.15, 0.38$ , and  $0.51$ ), which gradually weaken with increasing redshifts at  $z = 0.698$  and  $z = 2.334$  respectively. Interestingly, at  $z = 1.48$ , the direction of the correlation notably shifts. The red ellipsoids correspond to the Planck  $\Lambda$ CDM best-fit predictions. The consistent overlap between the blue and red regions at lower redshifts affirms the  $\Lambda$ CDM model’s validity. In contrast, the lack of overlap at higher  $z$  presents challenges to explaining background and perturbation observables within the standard cosmological framework. This calls for scrutiny to discern whether it indicates potential departures from the concordance model arising from genuine physical phenomena or the influence of unaccounted systematic effects.

#### 4.3. Comparison with Complementary Datasets

The whisker plot in Fig. 6 offers a comparative visualization of constraints on the  $\Lambda$ CDM model parameters:  $H_0$  (in units of  $\text{km Mpc}^{-1} \text{s}^{-1}$ ),  $\Omega_m$ ,  $\sigma_8$ , and  $S_8$ , derived from various state-of-the-art surveys in the overlapping redshift range  $z < 1.5$ . These include the results of our reconstruction at  $z = 0.15, 0.38, 0.51, 0.698$ , and  $1.48$  (referred to as “This Work”), constraints based on the SRG/eROSITA catalogues (Artis et al. 2024), the combination of ACT DR6 lensing + Planck PR4 + DESI BAO (Qu et al. 2024), and the DESI full-shape (Adame et al. 2024b) analysis. The  $1\sigma$  and  $2\sigma$  regions for all parameters based on the Planck baseline are illustrated in gray shades, while the  $H_0$  value from the SH0ES Collaboration is emphasized in orange. Each entry along the y-axis corresponds to a redshift bin associated with a specific dataset, while the horizontal error bars represent the uncertainty ranges for the respective parameters. Results obtained from our reconstruction are marked with blue circular markers, SRG/eROSITA with green downward triangles, (ACT DR6 + Planck PR4)  $\times$  DESI BAO with red squares, and DESI FS with purple upward triangles. The visualization highlights the ability of our cosmological model-agnostic MTGP framework to provide precise and competitive constraints on  $\Lambda$ CDM parameters. Each panel focuses on a specific cosmological parameter, illustrating different facets of the derived constraints.

- Our reconstruction results reveal a consistent trend of  $H_0$  increasing with decreasing  $z$  in the range  $0 < z < 1.48$ . In contrast, the DESI FS data exhibit an oscillating behavior in  $H_0$ , with the mean values alternately increasing and decreasing between  $z = 0.51, z = 0.706$ , and  $z = 0.930$ . Specifically, for DESI FS,  $H_0$  reaches the SH0ES value at  $z = 0.706$  but reverts to the Planck value at  $z = 0.930$ . At the remaining redshifts,  $H_0$  lies midway between the SH0ES and Planck results, stabilizing near  $\approx 70 \text{ km Mpc}^{-1} \text{s}^{-1}$ . From the SDSS data, we observe that at  $z = 0.698$ ,  $H_0$  closely aligns with the Planck

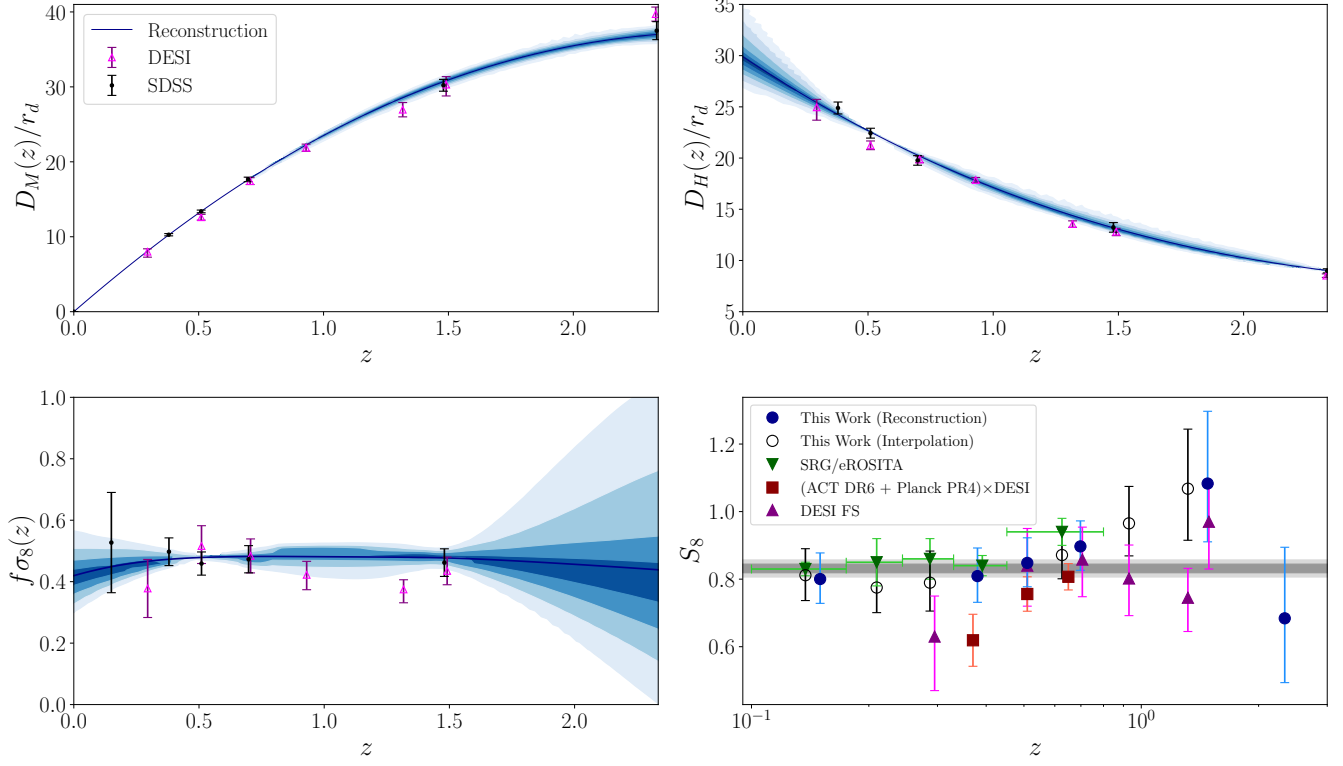


**Figure 7.** Plots showing a comparison among the reconstructed SDSS observables, observational data from SDSS BAO+RSD as well as DESI BAO+FS surveys. The top-left panel presents reconstruction of  $D_M(z)/r_d$  vs  $z$ , top-right panel shows  $D_H(z)/r_d$  vs  $z$ , and bottom right panel shows  $f\sigma_8(z)$  vs  $z$ . The bottom-right panel shows  $S_8$  values from MTGP reconstruction of SDSS BAO+RSD data, compared to SRG/eROSITA, ACT DR6+Planck PR4+DESI BAO, and DESI FS constraints assuming  $\Lambda$ CDM.

value, while at lower redshifts, such as  $z = 0.15$  and  $z = 0.38$ , it gets closer to the SHOES value or lies midway between SHOES and Planck.

- For  $\Omega_m$ , our reconstruction results indicate that the central values of  $\Omega_m$  increase with effective redshift. However, a constant  $\Omega_m$  remains consistent within  $1\sigma$  across the redshift range  $z < 1.48$ . This trend is also observed in the results from (ACT DR6 + Planck PR4)  $\times$  DESI BAO and DESI FS, where  $\Omega_m$  shows an increasing trend with  $z_{\text{eff}}$ , although a constant  $\Omega_m$  is permitted within  $2\sigma$ . In contrast, the SRG/eROSITA results exhibit an opposite trend, with  $\Omega_m$  decreasing as  $z$  increases, while still allowing for a constant  $\Omega_m$  within  $1\sigma$ .
- For  $\sigma_8$ , our reconstruction results, along with SRG/eROSITA and (ACT DR6 + Planck PR4)  $\times$  DESI, consistently show  $\sigma_8$  increasing with effective redshift. In the DESI FS data,  $\sigma_8$  follows a similar increasing trend up to  $z = 0.7$ , aligning with the trends observed in SDSS up to  $z = 0.698$ . However, beyond this,  $\sigma_8$  exhibits a decrease at  $z = 0.93$  and  $z = 1.317$ , coinciding with the oscillatory behavior observed in  $H_0$ . Since SDSS observations are not available in this redshift range, so definitive claims or comparisons cannot be made in this regard. Furthermore, we notice a sharp increase in  $\sigma_8$  at  $z = 1.491$  from DESI FS. Interestingly, this deviation seen at  $z = 1.491$  in DESI FS and at  $z = 1.48$  in SDSS exceeds the  $2\sigma$  statistical limit. This striking feature, appearing in multiple generations of BAO and RSD data, may hint at new physics. For SRG/eROSITA, a similar  $2\sigma$  deviation is observed in the  $z = 0.452 - 0.800$  range. This contrasts with the result at  $z = 0.65$  from (ACT DR6 + Planck PR4)  $\times$  DESI BAO, which remains consistent with the Planck  $\Lambda$ CDM prediction. For SDSS and DESI FS, at  $z = 0.698$  and  $z = 0.706$ , respectively, we observe similar trends, with  $\Lambda$ CDM just included within the  $1\sigma$  confidence level.
- For  $S_8$ , our reconstruction shows an increase with  $z_{\text{eff}}$ , a trend also observed for (ACT DR6 + Planck PR4)  $\times$  DESI BAO. For DESI FS,  $S_8$  initially increases with  $z_{\text{eff}}$  up to  $z = 0.706$ , then at  $z = 0.93$  and  $z = 1.317$ , it reverses direction and decreases as  $z$  increases. However, we observe a notable increase again at  $z = 1.48$ . This trend is also visible in SRG/eROSITA

results, where  $S_8$  remains fairly constant up to  $z < 0.452$ , after which it increases strikingly in the range  $0.425 < z < 0.825$ . For low redshift, at  $z = 0.295$  for DESI FS and  $z = 0.37$  for (ACT DR6 + Planck PR4)  $\times$  DESI BAO,  $S_8$  is significantly lower than the baseline Planck estimate, remaining within  $1\sigma$ . However, our reconstruction with SDSS and constraints from SRG/eROSITA show that the low- $z$  measurements align with the Planck estimate. At higher redshifts, though, both measurements show tension with Planck, with a deviation greater than  $1\sigma$ .

Fig. 7 showcases the reconstructed key cosmological observables in combination with SDSS BAO+RSD and DESI BAO+FS (Adame et al. 2024b) data. The top-left panel presents the reconstruction of  $D_M(z)/r_d$  as a function of redshift  $z$ . The top-right panel shows the reconstruction of  $D_H(z)/r_d$  vs redshift  $z$ . The bottom-left panel displays reconstructed  $f\sigma_8(z)$  over the same redshift range. The dark blue line represents the best-fit reconstruction from SDSS data, while the shaded regions denote the  $1\sigma$  and  $2\sigma$  confidence levels. The circle error bars in black correspond to SDSS data points, and the pink triangles represent data extracted from the DESI BAO+FS analysis. We undertake this comparison to understand the generic trends between the previous SDSS and the latest DESI datasets, exploring the implications of these trends in SDSS and follow up to investigate hints towards potential future trends in DESI. This includes examining how small differences between SDSS and DESI might affect the reconstruction of the functions, as a diagnostic check for the  $\Lambda$ CDM model across redshifts in a data-driven manner.

- For  $D_M/r_d$ , the DESI low- $z$  measurements are consistent with SDSS data up to  $z = 1.491$ , where both values almost overlap, except for a minor dip observed at DESI QSO redshift  $z = 1.317$  from the final reconstruction curve obtained using SDSS data. However, at higher redshifts, a  $>2\sigma$  difference is observed in the case of the Ly- $\alpha$  tracer. This suggests that the reconstructed  $D_M/r_d$  from DESI data is expected to deviate from that of SDSS beyond  $z > 1.5$ , as the Ly- $\alpha$  data at  $z = 2.33$  will influence the training of MTGP hyperparameters. Consequently, this will lead to notable changes in the predicted values. The inferred  $D_M/r_d$  from DESI may be comparatively higher compared to those of SDSS for redshifts  $z > 1.5$ .
- The generic trend of  $D_H/r_d$  for both SDSS and DESI remains quite similar throughout the redshift range  $0 < z < 2.334$ . However, slight differences are observed between the two datasets. For DESI, the LRG1 tracer at  $z = 0.51$  yields a  $D_H/r_d$  value that is lower than the corresponding SDSS value by more than  $1\sigma$ . Similarly, at the DESI QSO tracer redshift  $z = 1.317$ ,  $D_H/r_d$  is found to be lower compared to the value obtained from the SDSS reconstruction. This suggests that future  $D_H/r_d$  measurements from DESI could result in a steeper slope of the curve at these redshifts compared to that of SDSS. Such deviations may hint at new features to investigate as observational data continue to become more refined.
- The  $f\sigma_8$  plot reveals interesting features: DESI exhibits an oscillatory behavior that is absent in SDSS, likely due to the fewer data points in the SDSS dataset. Nevertheless, both datasets remain consistent within  $1\sigma$ . The presence of such oscillatory behavior in DESI can lead to more pronounced wiggles in the reconstructed function compared to the smoother reconstruction derived from SDSS. Additionally, the DESI BGS tracer at  $z = 0.295$  shows a dip to lower values, suggesting that the reconstructed function will exhibit a larger dip at lower values compared to the current reconstruction based on SDSS MGS tracer data at  $z = 0.15$ .

The bottom-right panel of Fig. 7 presents the  $S_8$  values derived from MTGP reconstruction applied to SDSS data, with a LambdaCDM model fitted to the predicted constraints at each redshift bin. The panel also includes comparisons to constraints from SRG/eROSITA, ACT DR6 + Planck PR4 combined with DESI BAO, and DESI FS modeling, all assuming a LambdaCDM framework. The label 'This Work (Reconstruction)' represents the direct output of our reconstruction method at the SDSS effective redshifts, while 'This Work (Interpolation)' includes additional interpolated points to demonstrate the observed trends in  $S_8$ , highlighting its increase with effective redshift. Resulting constraints from SRG/eROSITA, ACT DR6 + Planck PR4 + DESI, and DESI FS are shown, emphasizing the competitive constraints provided by our methodology. To better capture the features at low- $z$ , the x-axis is scaled logarithmically. A general increasing trend in  $S_8$  is observed across all datasets. However, the value at  $z = 2.334$ , corresponding to the Ly- $\alpha$  measurement from the SDSS reconstruction, appears to be an outlier. Notably, there is no  $f\sigma_8$  measurement at this redshift, which limits its statistical significance.

## 5. CONCLUSION

The  $\Lambda$ CDM model, while phenomenologically successful in describing the dynamics of our Universe, remains a parameterized framework with no underlying theoretical explanation for its core components, such as dark energy and dark matter. However, tensions in model parameters—such as the  $> 5\sigma$  discrepancy in  $H_0$  between local and CMB measurements, and the  $\sim 2 - 2.5\sigma$  mismatch in  $S_8$  between CMB and weak lensing surveys—raise questions about its validity. These tensions, coupled with emerging

evidence for redshift-dependence in  $H_0$ ,  $\Omega_m$ , and  $S_8$ , suggest that either modifications to  $\Lambda$ CDM, its underlying assumptions are required, or unaccounted systematic effects when combining datasets must be addressed.

Traditional methods of stress-testing  $\Lambda$ CDM consistency across redshifts often rely on binning mechanisms, which inherently lose resolution and fail to capture subtle trends or correlations. In this work, we present a novel approach using the MTGP framework to reconstruct cosmological observables across redshifts, simultaneously probing both background ( $D_M/r_d$ ,  $D_H/r_d$ ) and perturbation ( $f\sigma_8$ ) sectors. Our analysis is based solely on SDSS-IV eBOSS data, incorporating the full covariance of the dataset, which includes auto-correlations of the same cosmological function and cross-correlations between different functions at various effective redshifts. By accounting for all systematics within the dataset and refraining from combining data from multiple surveys, we mitigate the influence of inter-survey systematics that could compromise the robustness of our results. This approach also avoids potential confirmation bias that can arise when datasets are combined under specific model assumptions, ensuring an unbiased evaluation of  $\Lambda$ CDM.

The MTGP framework offers several key advantages, making it a powerful tool for cosmological analysis. It is inherently model-independent, avoiding assumptions tied to specific cosmological models and enabling unbiased diagnostic tests. Integrating correlations between background and perturbation observables provides a unified and holistic view of cosmological trends. Unlike traditional binning approaches, which often obscure subtle variations, the MTGP framework captures smooth, high-resolution trends across redshifts, revealing potential inconsistencies that might otherwise go unnoticed. The phase spaces generated through this approach further enhance its utility by visualizing the overlap between background and perturbation sectors, allowing for a detailed examination of inconsistencies and the evolution of features across redshifts.

Our results reveal trends in  $H_0$ ,  $\Omega_m$ ,  $\sigma_8$ , and  $S_8$  that both corroborate and challenge findings from existing literature. The observed redshift-dependent variations in  $H_0$  are consistent with those of Wong et al. (2020); Krishnan et al. (2020); Millon et al. (2020); Krishnan et al. (2021); Dainotti et al. (2021); Colgáin et al. (2022, 2024); Hu & Wang (2022); Jia et al. (2023); Vagnozzi (2023), supporting the notion of decreasing  $H_0$  with increasing  $z$ . For  $\Omega_m$ , we find an increase with  $z$ , which aligns with the trends observed by Colgáin et al. (2022, 2024); Risaliti & Lusso (2019); Lusso et al. (2020); Yang et al. (2020); Khadka & Ratra (2020); Pastén & Cárdenas (2023), although being compatible with studies like Dinda (2024); Artis et al. (2024); Adame et al. (2024b,c,a) at  $1\sigma$  that suggest no such evolution. Similarly, the parameters  $\sigma_8$  and/or  $S_8$  show evidence of evolution with redshift, agreeing with findings from Adil et al. (2023); Akarsu et al. (2024); Qu et al. (2024); Adame et al. (2024b); Artis et al. (2024), indicating that the amplitude of matter fluctuations changes over cosmic time, but contrasting with results from Poulin et al. (2023); Manna & Desai (2024); Abbott et al. (2022), which find no significant redshift-dependent variations in  $\sigma_8$  or  $S_8$ .

This method will be particularly relevant for ongoing surveys like DESI, which has already released precise measurements from full-shape modelling of galaxy clusters (Adame et al. 2024b). These results, along with DESI DR1 BAO analysis, indicate a preference for dynamical dark energy over  $\Lambda$ CDM, with  $\Lambda$ CDM being excluded at more than  $2\sigma$  in the Planck+DESI+Pantheon+, Planck+DESI+DES-SN5YR and Planck+DESI+Union3 analyses (Adame et al. 2024c,a). Additionally, upcoming surveys like Euclid (Blanchard et al. 2020) can provide us with separate measurements of  $f(z)$ ,  $\sigma_8(z)$ , and  $f\sigma_8(z)$ , by combining RSD measurements in the power spectrum and bispectrum (Gil-Marín et al. 2017) or with galaxy-galaxy lensing data (de la Torre et al. 2017; Shi et al. 2018; Jullo et al. 2019), thereby breaking the inherent degeneracy. So, the ability of our framework to simultaneously analyze both background and perturbation sectors will henceforth be crucial.

Finally, the growing importance of redshift-dependent studies in cosmology highlights the need for tools that can uncover subtle deviations from  $\Lambda$ CDM. MTGP-based reconstruction sets the stage for future investigations, paving the way for exploring new physics while maintaining robustness against systematic uncertainties inherent in multi-survey combinations.

<sup>1</sup> We are grateful to Shadab Alam, Eoin Ó Colgáin, Shahin Sheikh Jabbari and Özgür Akarsu for useful discussions. PM  
<sup>2</sup> acknowledges funding from the Anusandhan National Research Foundation (ANRF), Govt of India under the National Post-  
<sup>3</sup> Doctoral Fellowship (File no. PDF/2023/001986). AAS acknowledges the funding from ANRF, Govt of India under the research  
<sup>4</sup> grant no. CRG/2023/003984. We acknowledge the use of HPC facility, Pegasus, at IUCAA, Pune, India. This article/publication  
<sup>5</sup> is based upon work from COST Action CA21136 – “Addressing observational tensions in cosmology with systematics and  
<sup>6</sup> fundamental physics (CosmoVerse)”, supported by COST (European Cooperation in Science and Technology).

*Software:* numpy (Harris et al. 2020), scipy (Virtanen et al. 2020), matplotlib (Hunter 2007), jax (Bradbury et al. 2018) tinygp (Foreman-Mackey et al. 2024), numpyro (Phan et al. 2019; Bingham et al. 2019), cobaya (Torrado & Lewis 2021), GetDist (Lewis 2019), fgivenx (Handley 2018)

## REFERENCES

- Abbott, T. M. C., et al. 2022, *Phys. Rev. D*, 105, 023520, doi: [10.1103/PhysRevD.105.023520](https://doi.org/10.1103/PhysRevD.105.023520)
- . 2024, *Astrophys. J. Lett.*, 973, L14, doi: [10.3847/2041-8213/ad6f9f](https://doi.org/10.3847/2041-8213/ad6f9f)
- Abdalla, E., et al. 2022, *JHEAp*, 34, 49, doi: [10.1016/j.jheap.2022.04.002](https://doi.org/10.1016/j.jheap.2022.04.002)
- Adame, A. G., et al. 2024a. <https://arxiv.org/abs/2404.03002>
- . 2024b. <https://arxiv.org/abs/2411.12021>
- . 2024c. <https://arxiv.org/abs/2411.12022>
- Ade, P. A. R., et al. 2016, *Astron. Astrophys.*, 594, A14, doi: [10.1051/0004-6361/201525814](https://doi.org/10.1051/0004-6361/201525814)
- Adil, S. A., Akarsu, O., Malekjani, M., et al. 2023, *Mon. Not. Roy. Astron. Soc.*, 528, L20, doi: [10.1093/mnras/slad165](https://doi.org/10.1093/mnras/slad165)
- Aghanim, N., et al. 2020, *Astron. Astrophys.*, 641, A6, doi: [10.1051/0004-6361/201833910](https://doi.org/10.1051/0004-6361/201833910)
- Aiola, S., et al. 2020, *JCAP*, 12, 047, doi: [10.1088/1475-7516/2020/12/047](https://doi.org/10.1088/1475-7516/2020/12/047)
- Akarsu, O., Colgáin, E. O., Sen, A. A., & Sheikh-Jabbari, M. M. 2024. <https://arxiv.org/abs/2410.23134>
- Akerib, D. S., et al. 2017, *Phys. Rev. Lett.*, 118, 021303, doi: [10.1103/PhysRevLett.118.021303](https://doi.org/10.1103/PhysRevLett.118.021303)
- Alam, S., et al. 2017, *Mon. Not. Roy. Astron. Soc.*, 470, 2617, doi: [10.1093/mnras/stx721](https://doi.org/10.1093/mnras/stx721)
- . 2021, *Phys. Rev. D*, 103, 083533, doi: [10.1103/PhysRevD.103.083533](https://doi.org/10.1103/PhysRevD.103.083533)
- Artis, E., et al. 2024. <https://arxiv.org/abs/2410.09499>
- Aubourg, E., et al. 2015, *Phys. Rev. D*, 92, 123516, doi: [10.1103/PhysRevD.92.123516](https://doi.org/10.1103/PhysRevD.92.123516)
- Bautista, J. E., et al. 2020, *Mon. Not. Roy. Astron. Soc.*, 500, 736, doi: [10.1093/mnras/staa2800](https://doi.org/10.1093/mnras/staa2800)
- Betoule, M., et al. 2014, *Astron. Astrophys.*, 568, A22, doi: [10.1051/0004-6361/201423413](https://doi.org/10.1051/0004-6361/201423413)
- Bingham, E., Chen, J. P., Jankowiak, M., et al. 2019, *J. Mach. Learn. Res.*, 20, 28:1. <http://jmlr.org/papers/v20/18-403.html>
- Blanchard, A., Héloret, J.-Y., Ilić, S., Lamine, B., & Tutusaus, I. 2024, *Open J. Astrophys.*, 7, 117170, doi: [10.33232/001c.117170](https://doi.org/10.33232/001c.117170)
- Blanchard, A., et al. 2020, *Astron. Astrophys.*, 642, A191, doi: [10.1051/0004-6361/202038071](https://doi.org/10.1051/0004-6361/202038071)
- Bonilla, E. V., Chai, K., & Williams, C. 2007, in *Advances in Neural Information Processing Systems*, ed. J. Platt, D. Koller, Y. Singer, & S. Roweis, Vol. 20 (Curran Associates, Inc.). [https://proceedings.neurips.cc/paper\\_files/paper/2007/file/66368270ffd51418ec58bd793f2d9b1b-Paper.pdf](https://proceedings.neurips.cc/paper_files/paper/2007/file/66368270ffd51418ec58bd793f2d9b1b-Paper.pdf)
- Boylan-Kolchin, M. 2023, *Nature Astron.*, 7, 731, doi: [10.1038/s41550-023-01937-7](https://doi.org/10.1038/s41550-023-01937-7)
- Bradbury, J., Frostig, R., Hawkins, P., et al. 2018, JAX: composable transformations of Python+NumPy programs, 0.3.13. <http://github.com/google/jax>
- Brieden, S., Gil-Marín, H., & Verde, L. 2023, *JCAP*, 04, 023, doi: [10.1088/1475-7516/2023/04/023](https://doi.org/10.1088/1475-7516/2023/04/023)
- Brout, D., et al. 2022, *Astrophys. J.*, 938, 110, doi: [10.3847/1538-4357/ac8e04](https://doi.org/10.3847/1538-4357/ac8e04)
- Bull, P., et al. 2016, *Phys. Dark Univ.*, 12, 56, doi: [10.1016/j.dark.2016.02.001](https://doi.org/10.1016/j.dark.2016.02.001)
- Carroll, S. M. 2001, *Living Rev. Rel.*, 4, 1, doi: [10.12942/lrr-2001-1](https://doi.org/10.12942/lrr-2001-1)
- Caruana, R. 1998, *Multitask Learning*, ed. S. Thrun & L. Pratt (Boston, MA: Springer US), 95–133, doi: [10.1007/978-1-4615-5529-2\\_5](https://doi.org/10.1007/978-1-4615-5529-2_5)
- Colgáin, E. O., Sheikh-Jabbari, M. M., Solomon, R., et al. 2022, *Phys. Rev. D*, 106, L041301, doi: [10.1103/PhysRevD.106.L041301](https://doi.org/10.1103/PhysRevD.106.L041301)
- Colgáin, E. O., Sheikh-Jabbari, M. M., Solomon, R., Dainotti, M. G., & Stojkovic, D. 2024, *Phys. Dark Univ.*, 44, 101464, doi: [10.1016/j.dark.2024.101464](https://doi.org/10.1016/j.dark.2024.101464)
- Dainotti, M. G., De Simone, B., Schiavone, T., et al. 2021, *Astrophys. J.*, 912, 150, doi: [10.3847/1538-4357/abe673](https://doi.org/10.3847/1538-4357/abe673)
- de la Torre, S., et al. 2017, *Astron. Astrophys.*, 608, A44, doi: [10.1051/0004-6361/201630276](https://doi.org/10.1051/0004-6361/201630276)
- de Mattia, A., et al. 2021, *Mon. Not. Roy. Astron. Soc.*, 501, 5616, doi: [10.1093/mnras/staa3891](https://doi.org/10.1093/mnras/staa3891)
- Di Valentino, E., et al. 2021a, *Astropart. Phys.*, 131, 102605, doi: [10.1016/j.astropartphys.2021.102605](https://doi.org/10.1016/j.astropartphys.2021.102605)
- . 2021b, *Astropart. Phys.*, 131, 102604, doi: [10.1016/j.astropartphys.2021.102604](https://doi.org/10.1016/j.astropartphys.2021.102604)
- Di Valentino, E., Mena, O., Pan, S., et al. 2021c, *Class. Quant. Grav.*, 38, 153001, doi: [10.1088/1361-6382/ac086d](https://doi.org/10.1088/1361-6382/ac086d)
- Dinda, B. R. 2024, *Eur. Phys. J. C*, 84, 402, doi: [10.1140/epjc/s10052-024-12774-x](https://doi.org/10.1140/epjc/s10052-024-12774-x)
- Dinda, B. R., & Maartens, R. 2024. <https://arxiv.org/abs/2407.17252>
- du Mas des Bourboux, H., et al. 2020, *Astrophys. J.*, 901, 153, doi: [10.3847/1538-4357/abb085](https://doi.org/10.3847/1538-4357/abb085)
- Efstathiou, G. 2024. <https://arxiv.org/abs/2406.12106>
- Eisenstein, D. J., & Hu, W. 1998, *Astrophys. J.*, 496, 605, doi: [10.1086/305424](https://doi.org/10.1086/305424)



- Foreman-Mackey, D., Yu, W., Yadav, S., et al. 2024, *dfm/tinygp*: The tiniest of Gaussian Process libraries, v0.3.0, Zenodo, doi: [10.5281/zenodo.10463641](https://doi.org/10.5281/zenodo.10463641)
- Freedman, W. L., & Madore, B. F. 2023, *JCAP*, 11, 050, doi: [10.1088/1475-7516/2023/11/050](https://doi.org/10.1088/1475-7516/2023/11/050)
- Gaitskell, R. J. 2004, *Ann. Rev. Nucl. Part. Sci.*, 54, 315, doi: [10.1146/annurev.nucl.54.070103.181244](https://doi.org/10.1146/annurev.nucl.54.070103.181244)
- Gil-Marín, H., Percival, W. J., Verde, L., et al. 2017, *Mon. Not. Roy. Astron. Soc.*, 465, 1757, doi: [10.1093/mnras/stw2679](https://doi.org/10.1093/mnras/stw2679)
- Gil-Marín, H., et al. 2020, *Mon. Not. Roy. Astron. Soc.*, 498, 2492, doi: [10.1093/mnras/staa2455](https://doi.org/10.1093/mnras/staa2455)
- Guzzo, L., Strauss, M. A., Fisher, K. B., Giovanelli, R., & Haynes, M. P. 1997, *Astrophys. J.*, 489, 37, doi: [10.1086/304788](https://doi.org/10.1086/304788)
- Handley, W. 2018, *The Journal of Open Source Software*, 3, doi: [10.21105/joss.00849](https://doi.org/10.21105/joss.00849)
- Haridasu, B. S., Luković, V. V., Moresco, M., & Vittorio, N. 2018, *JCAP*, 10, 015, doi: [10.1088/1475-7516/2018/10/015](https://doi.org/10.1088/1475-7516/2018/10/015)
- Harris, C. R., Millman, K. J., van der Walt, S. J., et al. 2020, *Nature*, 585, 357–362, doi: [10.1038/s41586-020-2649-2](https://doi.org/10.1038/s41586-020-2649-2)
- Hazra, D. K., Majumdar, S., Pal, S., Panda, S., & Sen, A. A. 2015, *Phys. Rev. D*, 91, 083005, doi: [10.1103/PhysRevD.91.083005](https://doi.org/10.1103/PhysRevD.91.083005)
- Heymans, C., et al. 2021, *Astron. Astrophys.*, 646, A140, doi: [10.1051/0004-6361/202039063](https://doi.org/10.1051/0004-6361/202039063)
- Holsclaw, T., Alam, U., Sansó, B., et al. 2010, *Phys. Rev. Lett.*, 105, 241302, doi: [10.1103/PhysRevLett.105.241302](https://doi.org/10.1103/PhysRevLett.105.241302)
- . 2011, *Phys. Rev. D*, 84, 083501, doi: [10.1103/PhysRevD.84.083501](https://doi.org/10.1103/PhysRevD.84.083501)
- Hou, J., et al. 2020, *Mon. Not. Roy. Astron. Soc.*, 500, 1201, doi: [10.1093/mnras/staa3234](https://doi.org/10.1093/mnras/staa3234)
- Howlett, C., Ross, A., Samushia, L., Percival, W., & Manera, M. 2015, *Mon. Not. Roy. Astron. Soc.*, 449, 848, doi: [10.1093/mnras/stu2693](https://doi.org/10.1093/mnras/stu2693)
- Hu, J.-P., & Wang, F. Y. 2022, *Mon. Not. Roy. Astron. Soc.*, 517, 576, doi: [10.1093/mnras/stac2728](https://doi.org/10.1093/mnras/stac2728)
- Hunter, J. D. 2007, *Computing in Science & Engineering*, 9, 90, doi: [10.1109/MCSE.2007.55](https://doi.org/10.1109/MCSE.2007.55)
- Jia, X. D., Hu, J. P., & Wang, F. Y. 2023, *Astron. Astrophys.*, 674, A45, doi: [10.1051/0004-6361/202346356](https://doi.org/10.1051/0004-6361/202346356)
- Jullo, E., et al. 2019, *Astron. Astrophys.*, 627, A137, doi: [10.1051/0004-6361/201834629](https://doi.org/10.1051/0004-6361/201834629)
- Kaiser, N. 1987, *Mon. Not. Roy. Astron. Soc.*, 227, 1, doi: [10.1093/mnras/227.1.1](https://doi.org/10.1093/mnras/227.1.1)
- Khadka, N., & Ratra, B. 2020, *Mon. Not. Roy. Astron. Soc.*, 497, 263, doi: [10.1093/mnras/staa1855](https://doi.org/10.1093/mnras/staa1855)
- Krishnan, C., Colgáin, E. O., Ruchika, et al. 2020, *Phys. Rev. D*, 102, 103525, doi: [10.1103/PhysRevD.102.103525](https://doi.org/10.1103/PhysRevD.102.103525)
- Krishnan, C., Colgáin, E. O., Sheikh-Jabbari, M. M., & Yang, T. 2021, *Phys. Rev. D*, 103, 103509, doi: [10.1103/PhysRevD.103.103509](https://doi.org/10.1103/PhysRevD.103.103509)
- Krishnan, C., & Mondol, R. 2022, <https://arxiv.org/abs/2201.13384>
- Labbe, I., et al. 2023, *Nature*, 616, 266, doi: [10.1038/s41586-023-05786-2](https://doi.org/10.1038/s41586-023-05786-2)
- Lewis, A. 2019, <https://arxiv.org/abs/1910.13970>
- Li, X., et al. 2023, *Phys. Rev. D*, 108, 123518, doi: [10.1103/PhysRevD.108.123518](https://doi.org/10.1103/PhysRevD.108.123518)
- Lusso, E., et al. 2020, *Astron. Astrophys.*, 642, A150, doi: [10.1051/0004-6361/202038899](https://doi.org/10.1051/0004-6361/202038899)
- Manna, S., & Desai, S. 2024, *Eur. Phys. J. C*, 84, 661, doi: [10.1140/epjc/s10052-024-13031-x](https://doi.org/10.1140/epjc/s10052-024-13031-x)
- Millon, M., et al. 2020, *Astron. Astrophys.*, 639, A101, doi: [10.1051/0004-6361/201937351](https://doi.org/10.1051/0004-6361/201937351)
- Mukherjee, P. 2022, PhD thesis, IISER, Kolkata, <https://arxiv.org/abs/2207.07857>
- Mukherjee, P., & Sen, A. A. 2024, *Phys. Rev. D*, 110, 123502, doi: [10.1103/PhysRevD.110.123502](https://doi.org/10.1103/PhysRevD.110.123502)
- Neveux, R., et al. 2020, *Mon. Not. Roy. Astron. Soc.*, 499, 210, doi: [10.1093/mnras/staa2780](https://doi.org/10.1093/mnras/staa2780)
- Padmanabhan, T. 2003, *Phys. Rept.*, 380, 235, doi: [10.1016/S0370-1573\(03\)00120-0](https://doi.org/10.1016/S0370-1573(03)00120-0)
- Pastén, E., & Cárdenas, V. H. 2023, *Phys. Dark Univ.*, 40, 101224, doi: [10.1016/j.dark.2023.101224](https://doi.org/10.1016/j.dark.2023.101224)
- Patel, V., Chakraborty, A., & Amendola, L. 2024, <https://arxiv.org/abs/2407.06586>
- Payeur, G., McDonough, E., & Brandenberger, R. 2024, <https://arxiv.org/abs/2411.13637>
- Peebles, P. J. E. 2024, <https://arxiv.org/abs/2405.18307>
- Peebles, P. J. E., & Ratra, B. 2003, *Rev. Mod. Phys.*, 75, 559, doi: [10.1103/RevModPhys.75.559](https://doi.org/10.1103/RevModPhys.75.559)
- Peirone, S., Martinelli, M., Raveri, M., & Silvestri, A. 2017, *Phys. Rev. D*, 96, 063524, doi: [10.1103/PhysRevD.96.063524](https://doi.org/10.1103/PhysRevD.96.063524)
- Perenon, L., Martinelli, M., Ilić, S., et al. 2021, *Phys. Dark Univ.*, 34, 100898, doi: [10.1016/j.dark.2021.100898](https://doi.org/10.1016/j.dark.2021.100898)
- Perivolaropoulos, L., & Skara, F. 2022, *New Astron. Rev.*, 95, 101659, doi: [10.1016/j.newar.2022.101659](https://doi.org/10.1016/j.newar.2022.101659)
- Perlmutter, S., et al. 1999, *Astrophys. J.*, 517, 565, doi: [10.1086/307221](https://doi.org/10.1086/307221)
- Phan, D., Pradhan, N., & Jankowiak, M. 2019, arXiv preprint arXiv:1912.11554
- Poulin, V., Bernal, J. L., Kovetz, E. D., & Kamionkowski, M. 2023, *Phys. Rev. D*, 107, 123538, doi: [10.1103/PhysRevD.107.123538](https://doi.org/10.1103/PhysRevD.107.123538)
- Qu, F. J., et al. 2024, <https://arxiv.org/abs/2410.10808>
- Rasmussen, C., & Williams, C. 2006, *Gaussian processes for machine learning*, Vol. 2 (MIT Press), <https://gaussianprocess.org/gpml>
- Riess, A. G. 2019, *Nature Rev. Phys.*, 2, 10, doi: [10.1038/s42254-019-0137-0](https://doi.org/10.1038/s42254-019-0137-0)
- Riess, A. G., et al. 1998, *Astron. J.*, 116, 1009, doi: [10.1086/300499](https://doi.org/10.1086/300499)

- . 2022, *Astrophys. J. Lett.*, 934, L7,  
doi: [10.3847/2041-8213/ac5c5b](https://doi.org/10.3847/2041-8213/ac5c5b)
- Risaliti, G., & Lusso, E. 2019, *Nature Astron.*, 3, 272,  
doi: [10.1038/s41550-018-0657-z](https://doi.org/10.1038/s41550-018-0657-z)
- Sahni, V., & Starobinsky, A. A. 2000, *Int. J. Mod. Phys. D*, 9, 373,  
doi: [10.1142/S0218271800000542](https://doi.org/10.1142/S0218271800000542)
- Scolnic, D. M., et al. 2018, *Astrophys. J.*, 859, 101,  
doi: [10.3847/1538-4357/aab9bb](https://doi.org/10.3847/1538-4357/aab9bb)
- Seikel, M., Clarkson, C., & Smith, M. 2012, *JCAP*, 06, 036,  
doi: [10.1088/1475-7516/2012/06/036](https://doi.org/10.1088/1475-7516/2012/06/036)
- Shafieloo, A., Kim, A. G., & Linder, E. V. 2012, *Phys. Rev. D*, 85,  
123530, doi: [10.1103/PhysRevD.85.123530](https://doi.org/10.1103/PhysRevD.85.123530)
- Shi, F., et al. 2018, *Astrophys. J.*, 861, 137,  
doi: [10.3847/1538-4357/aacb20](https://doi.org/10.3847/1538-4357/aacb20)
- Tamone, A., et al. 2020, *Mon. Not. Roy. Astron. Soc.*, 499, 5527,  
doi: [10.1093/mnras/staa3050](https://doi.org/10.1093/mnras/staa3050)
- Torrado, J., & Lewis, A. 2021, *JCAP*, 05, 057,  
doi: [10.1088/1475-7516/2021/05/057](https://doi.org/10.1088/1475-7516/2021/05/057)
- Tristram, M., et al. 2024, *Astron. Astrophys.*, 682, A37,  
doi: [10.1051/0004-6361/202348015](https://doi.org/10.1051/0004-6361/202348015)
- Vagnozzi, S. 2023, *Universe*, 9, 393, doi: [10.3390/universe9090393](https://doi.org/10.3390/universe9090393)
- Verde, L., Treu, T., & Riess, A. G. 2019, *Nature Astron.*, 3, 891,  
doi: [10.1038/s41550-019-0902-0](https://doi.org/10.1038/s41550-019-0902-0)
- Virtanen, P., Gommers, R., Oliphant, T. E., et al. 2020, *Nature Methods*, 17, 261, doi: [10.1038/s41592-019-0686-2](https://doi.org/10.1038/s41592-019-0686-2)
- Weinberg, S. 1989, *Rev. Mod. Phys.*, 61, 1,  
doi: [10.1103/RevModPhys.61.1](https://doi.org/10.1103/RevModPhys.61.1)
- Wong, K. C., et al. 2020, *Mon. Not. Roy. Astron. Soc.*, 498, 1420,  
doi: [10.1093/mnras/stz3094](https://doi.org/10.1093/mnras/stz3094)
- Yang, T., Banerjee, A., & Colgáin, E. O. 2020, *Phys. Rev. D*, 102,  
123532, doi: [10.1103/PhysRevD.102.123532](https://doi.org/10.1103/PhysRevD.102.123532)